Robust phased-array radio system aided inertial navigation using factor graph optimisation

Glen Hjelmerud Mørkbak Sørensen, Torleiv H. Bryne, Kristoffer Gryte, Trym Synnevåg and Tor A. Johansen

***Abstract*— Global navigation satellite systems (GNSS) is the gold standard for aiding of inertial navigation systems (INS), but is highly susceptible to naturally occurring, unintentional, and intentional interference due to its low signal power. GNSS is also not suitable for use indoors or in other areas where the signal is blocked. In recent years, phased-array radio systems (PARS) have shown to have potential for navigation. After Bluetooth introduced direction finding in its specification, the technology has emerged as a low-cost PARS-based alternative. In this paper, an estimation scheme fusing PARS and inertial sensor data based on factor graph optimisation (FGO) using incremental smoothing and mapping with fixed-lag smoothing is applied and compared against a standard error-state Kalman filter (ESKF) solution as a benchmark. The results are obtained from 100 Monte Carlo runs of a simulated USV trajectory, where performance is compared when aided by both fault-free and erroneous PARS measurements, with and without robust estimation schemes. We find that our estimator slightly outperforms ESKF in North-East position and roll/pitch estimates, but struggles more with Down-position and yaw angle, possibly due to additional cross-covariance available to the ESKF.**

***Index Terms*— GNSS-denied navigation, phased-array radio systems (PARS), factor graph optimisation, autonomous systems**

I. Introduction

In autonomous navigation, an inertial navigation system (INS) is typically aided by position measurements from global navigation satellite systems (GNSS) to estimate the navigation state, where INS and GNSS are complementary [1]. However, depending on the area of application, problems may arise due to GNSS being prone to naturally occurring interference from e.g., ionospheric events or intentional interference such as jamming and spoofing [2]. In these environments, the state of the art has been an INS aided by vision-based systems [3]. These systems can provide great performance, but require sufficiently feature-rich environments, are computationally intensive, and may experience issues in degraded visual conditions.

In recent years, phased-array radio systems (PARS) have emerged as both a complementary navigation system to GNSS for redundancy purposes [4], [5], as well as an alternative [6], [7]. PARS measurements, however, also have their own issues that must be accounted for, with perhaps the most notable issue being multipath errors due to reflections off reflective surfaces causing the signal to be received via multiple paths by the receiver [8], [9]. Since the introduction of direction finding in the Bluetooth 5.1 specification [10], the use of low-cost PARS measurements for aided navigation has become an increasingly active area of research, with experimental results demonstrating the ability to perform unmanned aerial vehicle (UAV) navigation using Bluetooth Low Energy (BLE) PARS Angle-of-Arrival (AoA) measurements up to $700\,\mathrm{m}$ away from a base station [11]. In [4]–[8], [12], some variants of nonlinear observers and an error-state Kalman filter (ESKF)-based estimator were used. In recent years, the use of factor graph-based optimisation (FGO) in inertial navigation applications has become more widespread, with examples including e.g., visual-inertial odometry (VIO) in Forster et al. [13]. Furthermore, FGO facilitates multi-sensor fusion and simultaneous localisation and mapping (SLAM), with various VIO-based SLAM systems summarised in Dellaert and Kaess [14]. An example of FGO applied to LIDAR-aided inertial navigation is presented in Brossard et al. [15], whilst Siemuri et al. present a FGO-based positioning algorithm fusing smartphone GNSS measurements with inertial measurements [16].

A. Main contributions

The main contributions of this paper are as follows:

- We introduce a novel estimation scheme integrating PARS range, azimuth, and elevation measurements with measurements from an inertial measurement unit (IMU) using fixed-lag incremental smoothing and mapping based on iSAM2. The scheme handles outliers with the natural test or M-estimators.
- We compare the estimator to a benchmark ESKF estimator through 100 Monte Carlo simulations, testing performance under nominal and faulty PARS conditions, with and without robust estimation/outlier rejection.

The work is developed with BLE PARS in mind, although the PARS models used are generic. We provide the source code and scripts used in our study in an accompanying GitHub repository [17].

B. Organisation of the paper

The remainder of this paper is organised as follows. Sec. II covers preliminaries. Sec. III presents the preintegration theory and PARS factors used in the FGO scheme in this work, whilst the robust estimation schemes used are presented in Sec. IV. Sec. V presents the simulated experiment setup, with results presented and discussed in Sec. VI. Finally, the research will be summarised and concluded in Sec. VII.

the work is supported by the research council of norway through the project phased-array radio systems for resilient localization and navigation of autonomous systems in gnss-denied environments parnav (no. 338789)

The authors are with the Department of Engineering Cybernetics, Norwegian University of Science and Technology (NTNU), NO-7491 Trondheim, Norway. Corresponding author e-mail: glen.h.m.sorensen@ntnu.no

II. Preliminaries

A. Notation

The agent position is denoted with the vector of 3D-coordinates $\boldsymbol{p}$. The agent velocity, $\boldsymbol{v}$, is defined similarly, whilst the unit quaternion $\boldsymbol{q}$ is used to represent attitude. The accelerometer and gyroscope biases are given by $\boldsymbol{b}_{\text{acc}}$ and $\boldsymbol{b}_{\text{gyro}}$, respectively. The Hamiltonian quaternion convention is used and the quaternion product is denoted by $\otimes$ [18]. Matrices, in general, are given in bold face, capital letters, e.g., $\boldsymbol{M} \in \mathbb{R}^n$ of dimension n. $\boldsymbol{R}_a^b \in SO(3)$ denotes the rotation matrix that rotates vectors from coordinate frame $\{a\}$ to $\{b\}$, whilst $\boldsymbol{T}_a^b \in SE(3)$ denotes the homogeneous transformation matrix that transforms coordinate vectors between the two coordinate frames. Estimates of a variable x are denoted by $\hat{x}$. The matrix trace is given as $\text{tr}(\boldsymbol{M}) = \sum_{k=1}^{n} m_{kk}$. $\|\boldsymbol{u}\|_2$ denotes the Euclidean norm of the vector $\boldsymbol{u}$, whilst $[\boldsymbol{u}]_\times$ denotes its skew-symmetric matrix. The short-hand $\|\boldsymbol{u}\|_{\boldsymbol{P}}^2$ will be used to denote $\boldsymbol{u}^\top \boldsymbol{P}^{-1} \boldsymbol{u}$, where $\boldsymbol{P}$ is a symmetric, positive definite matrix. Finally, $\boldsymbol{u} \sim \mathcal{N}(\mu, \sigma^2)$ denotes a Gaussian distributed random variable with mean μ and variance σ^2, whilst $\boldsymbol{u} \sim \chi_n^2$ denotes a χ^2-distributed random variable with n degrees of freedom.

B. Coordinate frames

In this paper, $\{n\}$ denotes the North-East-Down (NED) coordinate frame, $\{b\}$ denotes the BODY coordinate frame, and $\{r\}$ denotes the radio system coordinate frame for a given BLE radio locator. Hence, with this notation the vector $\boldsymbol{p}_{rb}^n$ denotes the position of $\{b\}$ relative to $\{r\}$, decomposed in $\{n\}$.

C. Agent kinematics

The agent's navigation state vector $\boldsymbol{x} \triangleq [\boldsymbol{p}_{nb}^n \;\; \boldsymbol{v}_{nb}^n \;\; \boldsymbol{q}_b^n \;\; \boldsymbol{b}_{\text{acc}}^b \;\; \boldsymbol{b}_{\text{gyro}}^b]^\top \in \mathbb{R}^{16}$ is modelled using kinematics [13], [18]:

$$\begin{aligned}
\dot{\boldsymbol{p}}_{nb}^n &= \boldsymbol{v}_{nb}^n \\
\dot{\boldsymbol{v}}_{nb}^n &= \boldsymbol{R}_b^n(\boldsymbol{q}_b^n)(\boldsymbol{f}_{imu}^b - \boldsymbol{b}_{\text{acc}}^b - \boldsymbol{w}_v) + \boldsymbol{g}^n \\
\dot{\boldsymbol{q}}_b^n &= \frac{1}{2}\boldsymbol{q}_b^n \otimes (\boldsymbol{\omega}_{imu}^b - \boldsymbol{b}_{\text{gyro}}^b - \boldsymbol{w}_o) \\
\dot{\boldsymbol{b}}_{\text{acc}}^b &= -\frac{1}{\tau_{\text{acc}}}\boldsymbol{b}_{\text{acc}}^b + \boldsymbol{w}_{b_{\text{acc}}} \\
\dot{\boldsymbol{b}}_{\text{gyro}}^b &= -\frac{1}{\tau_{\text{gyro}}}\boldsymbol{b}_{\text{gyro}}^b + \boldsymbol{w}_{b_{\text{gyro}}},
\end{aligned} \tag{1}$$

where $\boldsymbol{g}^n \triangleq [0 \;\; 0 \;\; 9.81]^\top$. The expressions used for the true acceleration and angular velocity are obtained from solving for $\boldsymbol{f}_{nb}^n$ and $\boldsymbol{\omega}_{nb}^b$ in the measurement equations:

$$\begin{aligned}
\boldsymbol{f}_{imu}^b &= (\boldsymbol{R}_b^n)^\top(\boldsymbol{f}_{nb}^n - \boldsymbol{g}^n) + \boldsymbol{b}_{\text{acc}}^b + \boldsymbol{w}_v \\
\boldsymbol{\omega}_{imu}^b &= \boldsymbol{\omega}_{nb}^b + \boldsymbol{b}_{\text{gyro}}^b + \boldsymbol{w}_o,
\end{aligned} \tag{2}$$

which is the standard IMU model used in e.g., [13].

The accelerometer and gyroscope biases are modelled as first-order Gauss Markov processes with their respective time constants τ_{acc} and τ_{gyro} [19], whilst the system process noise $\boldsymbol{w}$ is defined as $\boldsymbol{w} \triangleq [\boldsymbol{w}_v^\top \;\; \boldsymbol{w}_o^\top \;\; \boldsymbol{w}_{b_{\text{acc}}}^\top \;\; \boldsymbol{w}_{b_{\text{gyro}}}^\top]^\top \in \mathbb{R}^{12}$ where $\boldsymbol{w} \sim \mathcal{N}(\boldsymbol{0}, \boldsymbol{\mathcal{Q}})$ with power spectral density

$$\boldsymbol{\mathcal{Q}} = \text{diag}(\boldsymbol{q}_v, \boldsymbol{q}_o, \boldsymbol{q}_{b_{\text{acc}}}, \boldsymbol{q}_{b_{\text{gyro}}})^2 \in \mathbb{R}^{12\times 12}. \tag{3}$$

D. PARS measurement model

The PARS measurements received from the locator(s) will be on the form [20]

$$\begin{aligned}
\boldsymbol{z}_{\text{PARS}}^r &= \begin{bmatrix} \rho^r \\ \Psi^r \\ \alpha^r \end{bmatrix} = \begin{bmatrix} \|\boldsymbol{p}_{rb}^r\|_2 \\ \arctan2\left(p_{rb,y}^r, p_{rb,x}^r\right) \\ \arctan2\left(-p_{rb,z}^r, \bar{\rho}\right) \end{bmatrix} + \boldsymbol{\varepsilon} \\
&= \boldsymbol{h}_{\text{PARS}}(\boldsymbol{x}) + \boldsymbol{\varepsilon},
\end{aligned} \tag{4}$$

where $\boldsymbol{z}_{\text{PARS}} \in \mathbb{R}^3$, and ρ, $\bar{\rho}$, Ψ, and α are the range, horizontal range, azimuth angle, and elevation angle, respectively. Moreover, $\boldsymbol{\varepsilon} \sim \mathcal{N}(\boldsymbol{0}, \boldsymbol{\mathcal{R}}_{\text{PARS}})$, where

$$\boldsymbol{\mathcal{R}}_{\text{PARS}} = \text{diag}(\sigma_\rho^2, \; \sigma_\Psi^2, \; \sigma_\alpha^2) \in \mathbb{R}^{3\times 3}, \tag{5}$$

is the measurement noise covariance. In the ideal case, the observation $\boldsymbol{z}$ at a given time step will be the *stacked* vector of individual observations from each locator, $\boldsymbol{z} \in \mathbb{R}^{3N}$, where N is the number of locators.

For convenience, it is assumed that the PARS receiver on the agent is co-located with the IMU, resulting in no lever arm between them. Furthermore, we assume that the mounting angle relating $\{r\}$ and $\{n\}$ is known and we assume without loss of generality that $\boldsymbol{R}_r^n \triangleq \boldsymbol{I}_3$. In practice, we would need to estimate this angle through some form of calibration [21].

E. SE(3) matrix Lie group

The special Euclidean matrix Lie group $SE(3)$ consists of homogeneous transformation matrices on the form

$$\boldsymbol{T}_b^a = \boldsymbol{T}(\boldsymbol{R}_b^a, \; \boldsymbol{p}_{ab}^a) = \begin{bmatrix} \boldsymbol{R}_b^a & \boldsymbol{p}_{ab}^a \\ \boldsymbol{0}_{1\times 3} & 1 \end{bmatrix} \in SE(3), \tag{6}$$

with its inverse given by

$$(\boldsymbol{T}_b^a)^{-1} = \begin{bmatrix} (\boldsymbol{R}_b^a)^\top & -(\boldsymbol{R}_b^a)^\top \boldsymbol{p}_{ab}^a \\ \boldsymbol{0}_{1\times 3} & 1 \end{bmatrix} \in SE(3), \tag{7}$$

also in the same group [22].

Uncertainty can be associated to the pose $\boldsymbol{T}$ via

$$\boldsymbol{T} \triangleq \hat{\boldsymbol{T}} \exp(\boldsymbol{\xi}^\wedge) \triangleq \hat{\boldsymbol{T}} \; \text{Exp}(\boldsymbol{\xi}), \tag{8}$$

where $\hat{\boldsymbol{T}} \in SE(3)$ is the pose estimate and $\boldsymbol{\xi} = [\boldsymbol{\xi}_o \; \boldsymbol{\xi}_p]^\top \in \mathbb{R}^6$ is a local perturbation, where $\boldsymbol{\xi}_o$ is the rotation/orientation increment and $\boldsymbol{\xi}_p$ is the translation/position increment [22], [23]. The hat operator on $SE(3)$ is defined as

$$^\wedge\colon \mathbb{R}^6 \mapsto \mathfrak{se}(3) : \boldsymbol{\xi} \mapsto \begin{bmatrix} [\boldsymbol{\xi}_o]_\times & \boldsymbol{\xi}_p \\ \boldsymbol{0}_{1\times 3} & 0 \end{bmatrix}. \tag{9}$$

It maps $\boldsymbol{\xi}$ onto the *Lie algebra* $\mathfrak{se}(3)$ corresponding to $SE(3)$ [14]. *The capitalised exponential map*, $\text{Exp}(\boldsymbol{\xi})$, is thus defined as the matrix exponential of the mapped perturbation $\boldsymbol{\xi}^\wedge \in \mathfrak{se}(3)$

$$\begin{aligned}
\text{Exp}(\boldsymbol{\xi}) \triangleq \exp(\boldsymbol{\xi}^\wedge) &= \exp\left(\begin{bmatrix} [\boldsymbol{\xi}_o]_\times & \boldsymbol{\xi}_p \\ \boldsymbol{0}_{1\times 3} & 0 \end{bmatrix}\right) \\
&\approx \boldsymbol{I}_4 + \boldsymbol{\xi}^\wedge + \frac{1}{2!}(\boldsymbol{\xi}^\wedge)^2 + \ldots,
\end{aligned} \tag{10}$$

where the expressions are obtained from [22].

III. Factor graph-based optimisation

In this paper, the FGO problem will be solved using iSAM2 with fixed-lag smoothing [24] and be implemented

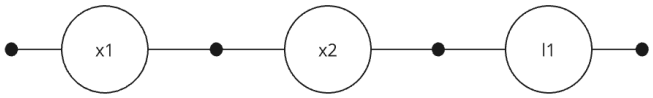

Fig. 1: Factor graph with two poses x_1 and x_2 and a landmark l_1. Example modified from introductory example in [14].

using GTSAM's combined IMU factor with on-manifold preintegration [25]–[27] and custom PARS factors. When FGO operates with fixed-lag smoothing, only factors that are connected to nodes within a window of time are kept in the graph for optimisation [14]. The reduction in size and complexity of the graph makes it suitable for real-time applications.

A. Factor graphs

Factor graphs are represented using a graphical modelling language well-suited to perform large-scale Maximum a Posteriori (MAP) inference. An example of a simple factor graph is shown in Fig. 1. Here, two robot poses (x_1, x_2) and a landmark l_1 are the variables of the graph, and there is a bearing measurement z relating l_1 to x_2. This graph can be expressed by the following factored function

$$\begin{aligned}\phi(X) &= \phi_1(x_1)\phi_2(x_2, x_1)\phi_3(l_1)\phi_4(x_2, l_1) \\ &= p(x_1)p(x_2|x_1)p(l_1)l(x_2, l_1; z),\end{aligned} \tag{11}$$

where $\phi_1(x_1)$ and $\phi_3(l_1)$ represent the prior densities of the robot pose and landmark, respectively, $\phi_2(x_2, x_1)$ represents the conditional probability density of the second pose on the first, $p(x_2|x_1)$, whilst $\phi_4(x_2, l_1)$ represents the likelihood $l(x_2, l_1; z)$. For a more formal definition of factor graphs, the reader is referred to Dellaert and Kaess [14].

B. The motivation behind custom PARS factors

GTSAM provides its own range- and bearing factors that could be applied in this context [28]. The motivation behind custom factors is threefold:

1) The provided factors are two-way factors, i.e., locator position is also estimated. This is known in our case.
2) With three factors, we can more pressingly address outlier rejection in the event only one of three measurements should be discarded.
3) The provided factors assume $\{b\}$-fixed measurements, we use $\{r\}$-fixed.

C. PARS factors

Generically, [14, Ch. 6.2] presents the pose optimisation

$$\hat{\boldsymbol{T}} = \arg\min_{\boldsymbol{T}} \|\boldsymbol{h}(\boldsymbol{T}) - \boldsymbol{z}\|^2_{\boldsymbol{\mathcal{P}}}. \tag{12}$$

To solve the problem w.r.t. the local perturbation $\boldsymbol{\xi}$, the problem is reformulated to

$$\hat{\boldsymbol{\xi}} \approx \arg\min_{\boldsymbol{\xi}} \|\boldsymbol{h}(\hat{\boldsymbol{T}}) + \boldsymbol{H}\boldsymbol{\xi} - \boldsymbol{z}\|^2_{\boldsymbol{\mathcal{P}}}, \tag{13}$$

where $\boldsymbol{H}$ is the measurement Jacobian w.r.t $\mathfrak{se}(3)$ and $\boldsymbol{\mathcal{P}}$ is the estimation error covariance.

The measurement Jacobians of (4) on $SE(3)$ are given by

$$\boldsymbol{H}_\rho = \frac{1}{\|\hat{\boldsymbol{p}}^n_{rb}\|_2}(\hat{\boldsymbol{p}}^n_{rb})^\top \boldsymbol{H}_p \tag{14a}$$

$$\boldsymbol{H}_\Psi = \frac{1}{\hat{p}_x^2 + \hat{p}_y^2}\begin{bmatrix}-\hat{p}_y & \hat{p}_x & 0\end{bmatrix}\boldsymbol{H}_p \tag{14b}$$

$$\boldsymbol{H}_\alpha = \frac{1}{\|\hat{\boldsymbol{p}}\|_2^2}\begin{bmatrix}\frac{p_x p_z}{\sqrt{\hat{p}_x^2+\hat{p}_y^2}} & \frac{p_y p_z}{\sqrt{\hat{p}_x^2+\hat{p}_y^2}} & -\sqrt{\hat{p}_x^2+\hat{p}_y^2}\end{bmatrix}\boldsymbol{H}_p, \tag{14c}$$

where $\boldsymbol{H}_p = \begin{bmatrix}\boldsymbol{0}_{3\times 3} & \hat{\boldsymbol{R}}^n_b\end{bmatrix}$ relates the position measured by the locator to $\mathfrak{se}(3)$. The derivations are given in Appx. I.

D. On-manifold IMU preintegration

We use the on-manifold IMU preintegration measurement model derived in [13]

$$\begin{aligned}\Delta\tilde{\boldsymbol{R}}_{ij} &= \boldsymbol{R}_i^\top \boldsymbol{R}_j \,\mathrm{Exp}(\boldsymbol{w}_o) \\ \Delta\tilde{\boldsymbol{v}}_{ij} &= \boldsymbol{R}_i^\top(\boldsymbol{v}_j - \boldsymbol{v}_i - \boldsymbol{g}\Delta t_{ij}) + \boldsymbol{w}_v \\ \Delta\tilde{\boldsymbol{p}}_{ij} &= \boldsymbol{R}_i^\top(\boldsymbol{p}_j - \boldsymbol{p}_i - \boldsymbol{v}_i\Delta t_{ij} - \frac{1}{2}\boldsymbol{g}\Delta {t_{ij}}^2) + \boldsymbol{w}_p,\end{aligned} \tag{15}$$

where $\boldsymbol{w}_p \sim \mathcal{N}(0, q^2_{\boldsymbol{p}})$ denotes the preintegrated measurement noise. Here, the left-hand side represents *compound measurements* obtained by integrating the IMU measurements between aiding measurements. Since it is the specific force vector measured by the accelerometers that is integrated, $\Delta\tilde{\boldsymbol{v}}_{ij}$ and $\Delta\tilde{\boldsymbol{p}}_{ij}$ do not represent true increments, although $\Delta\tilde{\boldsymbol{R}}_{ij}$ does.

E. State estimation

The FGO-based estimator maintains separate state- and covariance estimates of the pose, velocity, and IMU biases, i.e., $\hat{\boldsymbol{x}} \triangleq (\hat{\boldsymbol{T}}^n_b, \hat{\boldsymbol{v}}^n_{nb}, \hat{\boldsymbol{b}}^b) \in SE(3) \times \mathbb{R}^3 \times \mathbb{R}^6$, where $\hat{\boldsymbol{b}}^b \triangleq [\hat{\boldsymbol{b}}^{b,\top}_{\text{acc}} \;\; \hat{\boldsymbol{b}}^{b,\top}_{\text{gyro}}]^\top$. This means that the FGO-based estimator, unlike the ESKF (Appx. II), does not have access to cross-covariance between the elements of the pose and the velocity/biases. The pose and velocity estimates are propagated in between measurement updates using (15), whilst the bias estimates are updated whenever an optimisation is performed on the graph.

IV. Robust estimation

To test estimator performance when the PARS measurements are degraded or affected by sensor faults, two approaches will be examined: rejecting outliers using the *natural test* and de-weighting large outliers using two different *M-estimators*. The former will be applied to both estimators, whilst the latter will only be applied to the FGO-based estimator.

A. Rejecting outliers using the natural test

The natural test is based on the test statistic

$$T(z_{k,j}) = \|\boldsymbol{\nu}_{k,j}\|^2_{\mathcal{S}_{k,j}} \sim \chi^2_{1,\alpha},\; j \in \{1, ..., n_z\}, \tag{16}$$

where j and n_z are the given measurement and total number of measurements in the vector $\boldsymbol{z}_k$, respectively [29, Ch. 7.6.1], α is the confidence level of the test statistic, and $\boldsymbol{\nu}_k \triangleq \boldsymbol{z}_k - \boldsymbol{h}(\hat{\boldsymbol{x}}_k)$ and $\boldsymbol{\mathcal{S}}_k \triangleq \boldsymbol{H}\hat{\boldsymbol{\mathcal{P}}}_k\boldsymbol{H}^\top + \boldsymbol{\mathcal{R}}$ are the

innovation and *innovation covariance* of $\boldsymbol{z}_k$, respectively. A measurement should be rejected if T is greater than a threshold $T(z_{k,j}) > \chi^2_{1,\alpha}$. In practice, this results in the measurement j not being considered in the ESKF update, and not being added as a factor in the factor graph. In this paper, the ESKF update and natural test are implemented sequentially. This is enabled by a diagonal $\boldsymbol{\mathcal{R}}$-matrix.

B. De-weighting outliers using M-estimators

M-estimators are a class of estimators proposed by Huber in [30], designed to satisfy the following criteria: i) be reasonably efficient at the assumed model, ii) resistant to change in data, and iii) be robust against significant outliers [31]. In this paper, we will consider two M-estimators, the Huber M-estimator

$$Q(x) = \begin{cases} \frac{1}{2}x^2, & \text{for } |x| < k \\ k|x| - \frac{1}{2}k^2, & \text{otherwise,} \end{cases} \tag{17}$$

and the Tukey M-estimator

$$Q(x) = \begin{cases} \frac{c^2}{6}\left(1 - [1 - (x - (x/c)^2]^3\right), & \text{for } |x| \leq c \\ \frac{c^2}{6}, & \text{otherwise,} \end{cases} \tag{18}$$

the expressions of which are obtained from [32]. $Q(x)$ is an objective function of the residual x in the FGO which, in our application, will be the innovation of each component of $\boldsymbol{z}_k$. The derivative of $Q(x)$, $\frac{\partial}{\partial x}Q(x) \triangleq \Psi(x)$, is known as the *influence function* of the M-estimator. Compared to the binary nature of the natural test, M-estimators do not necessarily ignore all information from outliers. E.g., Huber will always weigh outliers to some extent, although Tukey will disregard large outliers completely.

V. Simulation Setup

This section will outline the setup of the simulated test case the estimation algorithm will be applied on. We compare our estimation scheme with the ESKF, since this is the industry standard.

A. Simulated scenario

The simulated test case is based on a modified example from the Marine Systems Simulator (MSS) toolbox [33]. The test case simulates a USV being disturbed by an ocean current whilst following a fixed, waypoint-generated path between two piers, each with a PARS locator mounted at a height of 12 m. The IMU has an update rate of 100 Hz, whilst aiding measurements are received at a rate of 10 Hz. The USV trajectory, as well as the locators and the Line-of-Sight (LOS) vector between them are shown in Fig. 2. Here, we note that the trajectory intersects the LOS between the locators at two points during a turn. The horizontal (North-East) and vertical (Down) dilution-of-precision (DOP) [1], denoted HDOP and VDOP, respectively, computed from the locators to ground truth are shown in Fig. 3. This is used to illustrate the impact of the locator geometry. The placement of the locators (one at each pier) is to ensure the best position uncertainty cf. Fig. 3 when position accuracy is most critical, i.e., during docking.

The following operating modes are examined:

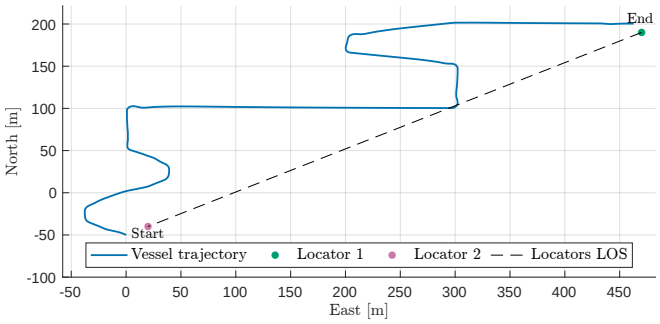

Fig. 2: USV trajectory between the two piers.

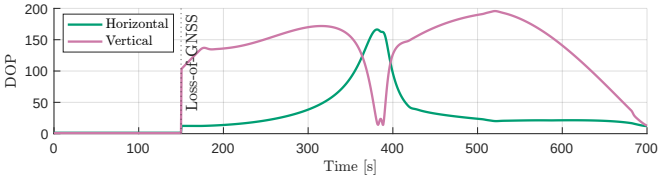

Fig. 3: Position dilution-of-precision (DOP) based on ground truth given by the localisation sensors (GNSS and PARS).

- Fault-free ESKF and FGO operation without any rejection or de-weighting of outliers.
- ESKF and FGO operation with unhandled sensor faults
- ESKF and FGO operation with outlier rejection based on the natural test, FGO will additionally be tested with the Huber and Tukey M-estimators.

The performance of each case is evaluated through 100 Monte Carlo runs. Here, 100 was chosen because it was deemed sufficient for providing representative statistics. In all cases, the estimator is run with GNSS position and compass measurements for 150 s before switching over to PARS aiding. This is primarily done to ensure that the estimates are reasonably stabilised before we compare the different scenarios, but it also mimics the loss-of-GNSS event which motivates the work.

B. Modelling PARS sensor faults

In this work, two types of faults will be considered: abnormal spikes affecting all measurements for a locator and multipath errors due to sea surface reflections affecting the elevation angle measurement. Furthermore, it is assumed that the faults are mutually exclusive for a given iteration k; if a spike is triggered for a given measurement, multipath will not be triggered and vice versa.

1) Modelling abnormal spikes: We define the following zero-mean Gaussian model $\boldsymbol{e}_\text{s} \sim \mathcal{N}(\boldsymbol{0}, k_s \cdot \boldsymbol{\mathcal{R}}_\text{PARS})$ with $k_s > 1$ chosen as $k_s = 2$ in the simulations to draw samples from whenever an abnormal spike fault is triggered, and modify the measurement model (4) as follows

$$\boldsymbol{z}_k = \boldsymbol{h}_k(\boldsymbol{x}_k) + \boldsymbol{e}_{\text{s},k} + \boldsymbol{\varepsilon}_k, \tag{19}$$

for the affected measurement at iteration k.

2) Modelling elevation angle multipath: We use a second-order Gauss-Markov process (SOGM) [19] to model the effect of multipath on the elevation angle measurement of a PARS locator. Whenever a multipath fault is triggered for a locator, we first determine how many consecutive

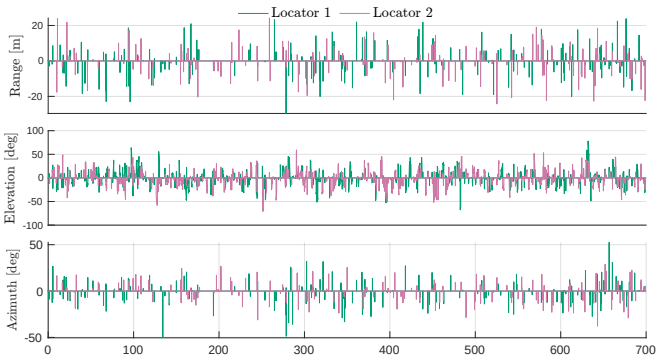

Fig. 4: Effect from sensor faults in run 88 out of 100.

measurements should be affected by drawing a sample d from a discrete uniform distribution $\mathcal{U}(3,\ 15)$, before we draw discrete-time samples b_k from the SOGM and modify the next d elevation angle measurements from the locator as follows

$$\boldsymbol{z}_{k,\alpha} = h_{k,\alpha} + b_k + \varepsilon_{k,\alpha}. \tag{20}$$

3) Resulting sensor fault setup in the simulated experiment: The effect of sensor faults on the PARS measurement in run 88 of 100 is shown in Fig. 4. Both spike and multipath error had a 3/100 chance to trigger for a given locator measurement at a given iteration k. With this setup, each locator had, on average, around 3% of measurements affected by spike errors and 24% affected by multipath errors in each run.

C. Evaluation criteria

To evaluate estimation performance, the mean Euclidean error norm averaged over the M runs was computed for the position and attitude. The error norm was compared against the corresponding 3σ-bound $U = 3\sqrt{\text{tr}(\hat{\boldsymbol{\mathcal{P}}})}$, obtained from the Frobenius norm of the corresponding subset of $\hat{\boldsymbol{\mathcal{P}}}$. In addition, the root mean square error (RMSE) from the M runs was computed for each individual component of $\boldsymbol{x}$ in (1), RMSE $\triangleq \sqrt{\frac{1}{N}\sum_{k=1}^{N} ||\boldsymbol{x} - \hat{\boldsymbol{x}}||_2^2}$, where N is the number of iterations in a given run.

D. Estimator tuning

The estimators were tuned one-to-one with the noise parameters used to generate measurements from sensors. The PARS and GNSS sensors were modelled generically, whilst the IMU was modelled as the STIM300 IMU [34]. The thresholds of the natural test and the M-estimators were kept at their recommended default levels. A table containing all tuning values can be found in the accompanying GitHub repo [17].

VI. Results and Discussion

A. Simulation results

The average RMSEs for each component of $\boldsymbol{x}$ in all operating modes tested are presented in Tab. I. The average estimation error norm of position and attitude over time, with corresponding 3σ-bounds, are shown in Fig. 5 for fault-free baselines, unhandled sensor faults (s.f.), and the natural

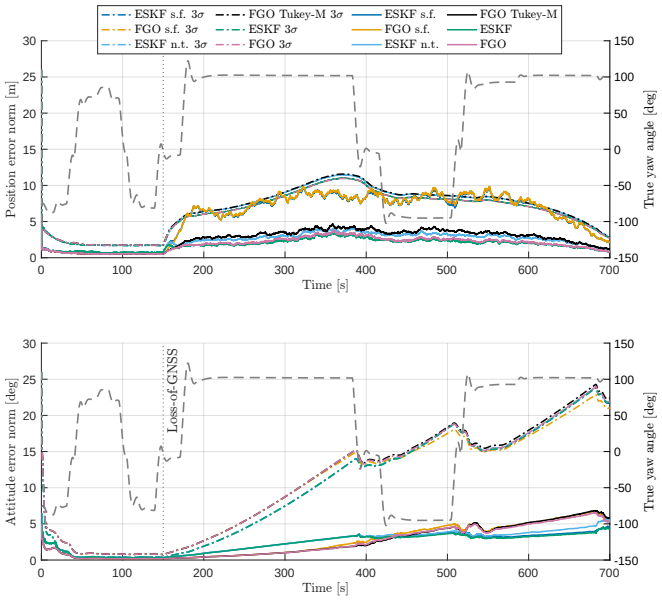

Fig. 5: **Left axis:** Average estimation error norm from 100 Monte Carlo runs in selected modes, plotted with respective 3σ-bounds over time. **Right axis:** True yaw angle over time, visualised by grey, dotted line.

test (n.t.) for the ESKF and Tukey M-estimator for FGO. Additionally, the true USV yaw angle is plotted to illustrate how turns affect estimation uncertainty.

1) Fault-free baseline: Both ESKF and FGO achieve comparable performance in estimating the USV position. The FGO obtains better North-East position estimates, but a worse Down-position estimate. The position estimation uncertainty increases after loss-of-GNSS and peaks halfway through the simulation. FGO initially retains a better attitude estimate over time, but is eventually overtaken by the ESKF. The FGO achieves better estimates of roll and pitch, but a worse estimate of the yaw. The attitude estimation uncertainty increases over time, but there are short-term improvements whenever the USV is turning. The general trend of better horizontal position estimation performance compared to the vertical axis is due to the localisation geometry of PARS locator setup. As seen from Fig. 3, HDOP is much lower than VDOP for most of the trajectory.

2) Unhandled sensor faults: Operating with unhandled PARS has a clear impact on on the position estimate, but a comparatively low impact on the attitude estimate. Furthermore, whilst all states are affected, the sensor faults mostly affect the Down-position (and velocity) and yaw estimates.

3) Rejecting outliers with the natural test: The position estimate is significantly improved when outliers are rejected with the natural test compared to when operating with unhandled faults, especially in Down-position. However, the natural test achieves worse attitude and gyroscope bias estimates, a result visible for the attitude error norm towards the end of the simulation.

4) De-weighting outliers with M-estimators: Aside from the baseline, the M-estimators (in particular Tukey) achieve the best estimate of North-East position. However, the Down-position estimate obtained here is noticeably worse than that

TABLE I: Average Root Mean Square Error (RMSE) after 100 Monte Carlo runs.

$M = 100$		$\boldsymbol{p}$ [m]			$\boldsymbol{v}$ [m/s]			$\boldsymbol{q}$ [deg]			$\boldsymbol{b}_{\text{acc}}$ [m/s^2]			$\boldsymbol{b}_{\text{gyro}}$ [deg/s]		
		N	E	D	N	E	D	Roll	Pitch	Yaw	x	y	z	Roll	Pitch	Yaw
ESKF	Fault-free	0.8962	1.3808	1.4410	0.2061	0.1721	0.1072	0.1902	0.5266	2.9402	0.0767	0.0236	0.0309	0.0259	0.0171	0.0299
	Sensor fault	1.0787	1.7237	7.7553	0.2267	0.1838	0.3362	0.1937	0.5280	3.0293	0.0767	0.0236	0.0317	0.0259	0.0172	0.0300
	Natural test	1.0546	1.6003	2.1382	0.2309	0.1919	0.1228	0.1965	0.5289	3.2476	0.0767	0.0237	0.0310	0.0259	0.0172	0.0304
FGO	Fault-free	0.8677	1.3824	1.6656	0.1977	0.1523	0.1276	0.1530	0.3365	3.4082	0.0563	0.0250	0.0303	0.0194	0.0163	0.0258
	Sensor fault	1.0459	1.6956	7.8407	0.2129	0.1640	0.3451	0.1548	0.3380	3.6179	0.0563	0.0250	0.0311	0.0194	0.0164	0.0262
	Natural test	1.0016	1.5948	2.5232	0.2228	0.1697	0.1439	0.1591	0.3394	3.8677	0.0563	0.0249	0.0304	0.0195	0.0164	0.0268
	Huber-M	0.9195	1.4645	3.9171	0.2001	0.1546	0.1916	0.1525	0.3368	3.4893	0.0564	0.0250	0.0305	0.0194	0.0163	0.0260
	Tukey-M	0.8997	1.4307	2.8297	0.1971	0.1525	0.1568	0.1517	0.3365	3.4518	0.0564	0.0250	0.0304	0.0193	0.0163	0.0259

of the natural test, which in turn negatively affects the error norm. Both M-estimators achieve improved angular estimates compared to FGO with the natural test, though the ESKF still achieves a better yaw estimate with unhandled faults.

B. Discussion

We highlight the following key results for discussion:

1) Yaw estimation error significantly larger than roll/pitch: None of the estimators are able to estimate the yaw as well as roll and pitch. Furthermore, the attitude error norm (where yaw will be the main contributor) starts increasing after loss-of-GNSS (and thus loss of GNSS-compass). This is perhaps not unexpected, given that the yaw angle is not in general directly observable.

2) FGO estimates North-East position and roll/pitch better, but Down-position and yaw worse: In the scenario tested, there is no change in Down-position over time and only changes in yaw during turns. If there is insufficient excitation in a state, and no direct measurement or motion constraints, the estimators must rely on cross-covariance terms with other states to improve these state estimates. Consequently, the ESKF may be outperforming the FGO-based estimator since it has access to the cross-covariance terms between the pose and velocity/bias states. Extending our estimation scheme to extended poses [15], $SE_2(3)$, where we would have access to the pose/velocity cross-covariance term, could potentially improve these estimates.

3) Position uncertainty reaches maximum around halfway through the simulation: The change in position uncertainty over time matches prior belief based on the USV trajectory and the HDOP cf. Fig. 3. The maximum is reached around the two points where the USV trajectory intersects the locators' LOS, which coincides with the max HDOP (worst geometry). Furthermore, we see that the position uncertainty improves as the USV is nearing the destination pier, where the HDOP is at its lowest after loss-of-GNSS.

4) Natural test yields worse attitude estimates than unhandled faults for both estimators: It is reasonable to assume that fewer outliers would improve the estimates, as is the case for the position estimate. The fact that the opposite is true for the attitude estimate (especially yaw) may be a result of non-faulty, noisy PARS measurements being rejected, resulting in less information for the estimators and – in turn – a worse estimate. Evidently, the effect of outliers on the angular estimates is negligible compared to those of the position. Furthermore, compared to unhandled faults, we also see an increase in the yaw gyro bias with the natural test. Here, performing a more controlled test where the test threshold is adjusted and the resulting number of false positives counted may be considered, in order to see if a more optimal threshold than the standard can be found.

5) M-estimators obtain worse D-position estimates than the natural test for FGO: For both ESKF and FGO, rejecting outliers improves the estimate of the Down-position considerably compared to operation with unhandled faults. Since the position is observable from the measurements, short periods without measurements such as what may be caused by outlier rejection may not cause much of an issue for the estimator, but if the threshold for de-weighting is set poorly for the application, the information from these outliers (or false positives) may do more harm than good. The Huber M-estimator is the worst performing out of all, whereas the Tukey M-estimator is far closer to the natural test. As previously mentioned, Huber will always weight outliers somewhat, whereas Tukey will ignore significant outliers. Similarly to the previous finding, a more thorough tuning process of the threshold values may improve the performance of the M-estimators. However, it is worth noting that aside from the baseline, the M-estimators (in particular, Tukey) obtain the best results for FGO for the North-East position estimate, and obtain the best angular estimates of the different FGO modes, which for an USV is more important than the Down-position.

VII. Conclusion

In this paper, a fixed-lag iSAM2 FGO estimator fusing PARS and IMU measurements was presented and tested against a benchmark ESKF estimator in 100 Monte Carlo runs of a simulated USV path between two piers, each with a PARS locator. Performance was compared in different operating modes: fault-free, unhandled faults, outlier rejection with natural test and (for the FGO) de-weighting of outliers with two types of M-estimators.

The results indicate that our estimation scheme, in particular when running with the Tukey M-estimator, slightly outperforms ESKF in North-East position and roll/pitch estimates, but struggles more with the estimate of the Down-position and yaw angle. We posit that the additional ESKF cross-covariance terms available compared to the FGO solution may be a reason for the more optimal ESKF estimates. The higher yaw estimation error in all modes is assumed to be a result of the yaw not being directly observable. Interestingly, better angular estimates are obtained with unhandled faults compared to outlier rejection with the natural test. This

may be due to suboptimal tuning of the robust estimation schemes applied resulting in useful data for the angular estimates being rejected due to non-faulty, albeit high, PARS noise.

Performing a more rigorous tuning process of the robust estimation schemes and testing the estimation scheme in other scenarios, including with experimental data, are part of the future work. Furthermore, extending the estimation scheme to $SE_2(3)$ to see whether the additional attitude/position-velocity cross-covariance terms obtained may improve the performance of the FGO-based estimator is also of interest.

APPENDIX I
COMPUTATION OF PARS JACOBIANS ON THE SE(3) MATRIX LIE GROUP

1) Agent position expressed using the Lie algebra: In order to compute the Jacobian of the PARS measurement model defined in (4) with respect to the Lie algebra $\mathfrak{se}(3)$ and get it on the form of (13), we must first express the agent position measured by a locator as a function $\boldsymbol{\xi}$, i.e.,

$$\boldsymbol{p}^n_{rb} \approx \hat{\boldsymbol{p}}^n_{rb} + \frac{\partial \boldsymbol{p}^n_{rb}}{\partial \boldsymbol{\xi}^\wedge}\boldsymbol{\xi} \triangleq \hat{\boldsymbol{p}}^n_{rb} + \boldsymbol{H}_p\boldsymbol{\xi}. \tag{21}$$

To obtain this expression, we start by expanding $\boldsymbol{p}^n_{rb}$ in homogeneous coordinates

$$\begin{aligned}
\begin{bmatrix}\boldsymbol{p}^n_{rb}\\ 1\end{bmatrix} &= \begin{bmatrix}-\boldsymbol{R}^n_b(\boldsymbol{R}^n_b)^\top(\boldsymbol{p}^n_{nr}-\boldsymbol{p}^n_{nb})\\ 1\end{bmatrix}\\
&= \begin{bmatrix}-\boldsymbol{R}^n_b & 0\\ 0 & 1\end{bmatrix}\begin{bmatrix}(\boldsymbol{R}^n_b)^\top(\boldsymbol{p}^n_{nr}-\boldsymbol{p}^n_{nb})\\ 1\end{bmatrix}\\
&= \begin{bmatrix}-\boldsymbol{R}^n_b & 0\\ 0 & 1\end{bmatrix}\begin{bmatrix}(\boldsymbol{R}^n_b)^\top & -(\boldsymbol{R}^n_b)^\top\boldsymbol{p}^n_{nb}\\ 0 & 1\end{bmatrix}\begin{bmatrix}\boldsymbol{p}^n_{nr}\\ 1\end{bmatrix}\\
&= \boldsymbol{T}(-\boldsymbol{R}^n_b,\ \boldsymbol{0})\boldsymbol{T}^{-1}(\boldsymbol{R}^n_b,\ \boldsymbol{p}^n_{nb})\begin{bmatrix}\boldsymbol{p}^n_{nr}\\ 1\end{bmatrix},
\end{aligned} \tag{22}$$

where $\boldsymbol{p}^n_{nr}$ is the known origin of $\{r\}$, i.e., the placement of the given locator, expressed in $\{n\}$.

Next, insert for (8)

$$\begin{aligned}
\begin{bmatrix}\boldsymbol{p}^n_{rb}\\ 1\end{bmatrix} =& \hat{\boldsymbol{T}}(-\hat{\boldsymbol{R}}^n_b, \boldsymbol{0})\ \mathrm{Exp}(\boldsymbol{\xi})\left(\hat{\boldsymbol{T}}(\hat{\boldsymbol{R}}^n_b, \hat{\boldsymbol{p}}^n_{nb})\ \mathrm{Exp}(\boldsymbol{\xi})\right)^{-1}\begin{bmatrix}\boldsymbol{p}^n_{nr}\\ 1\end{bmatrix}\\
=& \begin{bmatrix}-\hat{\boldsymbol{R}}^n_b\ \mathrm{Exp}(\boldsymbol{\xi}) & 0\\ 0 & 1\end{bmatrix}\ \mathrm{Exp}(-\boldsymbol{\xi})\\
&\begin{bmatrix}(\hat{\boldsymbol{R}}^n_b)^\top & -(\hat{\boldsymbol{R}}^n_b)^\top\hat{\boldsymbol{p}}^n_{nb}\\ 0 & 1\end{bmatrix}\begin{bmatrix}\boldsymbol{p}^n_{nr}\\ 1\end{bmatrix}\\
\overset{(10)}{\approx}& \begin{bmatrix}-\hat{\boldsymbol{R}}^n_b\,(\boldsymbol{I}_3+[\boldsymbol{\xi}_o]_\times) & 0\\ 0 & 1\end{bmatrix}\begin{bmatrix}(\boldsymbol{I}_3-[\boldsymbol{\xi}_o]_\times) & -\boldsymbol{\xi}_p\\ 0 & 1\end{bmatrix}\\
&\begin{bmatrix}(\hat{\boldsymbol{R}}^n_b)^\top & -(\hat{\boldsymbol{R}}^n_b)^\top\hat{\boldsymbol{p}}^n_{nb}\\ 0 & 1\end{bmatrix}\begin{bmatrix}\boldsymbol{p}^n_{nr}\\ 1\end{bmatrix}\\
=& \begin{bmatrix}-\hat{\boldsymbol{R}}^n_b\,(\boldsymbol{I}_3+[\boldsymbol{\xi}_o]_\times) & 0\\ 0 & 1\end{bmatrix}\begin{bmatrix}(\boldsymbol{I}_3-[\boldsymbol{\xi}_o]_\times) & -\boldsymbol{\xi}_p\\ 0 & 1\end{bmatrix}\\
&\begin{bmatrix}-(\hat{\boldsymbol{R}}^n_b)^\top(\hat{\boldsymbol{p}}^n_{nb}-\boldsymbol{p}^n_{nr})\\ 1\end{bmatrix}\\
=& \begin{bmatrix}-\hat{\boldsymbol{R}}^n_b+\hat{\boldsymbol{R}}^n_b[\boldsymbol{\xi}_o]^2_\times & \hat{\boldsymbol{R}}^n_b\boldsymbol{\xi}_p+\hat{\boldsymbol{R}}^n_b[\boldsymbol{\xi}_o]_\times\boldsymbol{\xi}_p\\ 0 & 1\end{bmatrix}\\
&\begin{bmatrix}-(\hat{\boldsymbol{R}}^n_b)^\top(\hat{\boldsymbol{p}}^n_{nb}-\boldsymbol{p}^n_{nr})\\ 1\end{bmatrix}.
\end{aligned} \tag{23}$$

The first-order approximation in (10) assumes that the perturbation $\boldsymbol{\xi}$ is small. Under the same assumption, the square and cross-terms of $\boldsymbol{\xi}$ are assumed to be negligible such that

$$\begin{aligned}
\begin{bmatrix}\boldsymbol{p}^n_{rb}\\ 1\end{bmatrix} &\approx \begin{bmatrix}-\hat{\boldsymbol{R}}^n_b & \hat{\boldsymbol{R}}^n_b\boldsymbol{\xi}_p\\ 0 & 1\end{bmatrix}\begin{bmatrix}-(\hat{\boldsymbol{R}}^n_b)^\top(\hat{\boldsymbol{p}}^n_{nb}-\boldsymbol{p}^n_{nr})\\ 1\end{bmatrix}\\
&= \begin{bmatrix}\hat{\boldsymbol{R}}^n_b(\hat{\boldsymbol{R}}^n_b)^\top(\hat{\boldsymbol{p}}^n_{nb}-\boldsymbol{p}^n_{nr})+\hat{\boldsymbol{R}}^n_b\boldsymbol{\xi}_p\\ 1\end{bmatrix}\\
&= \begin{bmatrix}\hat{\boldsymbol{p}}^n_{rb}\\ 1\end{bmatrix}+\begin{bmatrix}\boldsymbol{0}_{3\times3} & \hat{\boldsymbol{R}}^n_b\\ \boldsymbol{0}_{1\times3} & \boldsymbol{0}_{1\times3}\end{bmatrix}\begin{bmatrix}\boldsymbol{\xi}_o\\ \boldsymbol{\xi}_p\end{bmatrix}.
\end{aligned} \tag{24}$$

From this, we recognise the structure of (21)

$$\boldsymbol{p}^n_{rb} \approx \hat{\boldsymbol{p}}^n_{rb} + \underbrace{\begin{bmatrix}\boldsymbol{0}_{3\times3} & \hat{\boldsymbol{R}}^n_b\end{bmatrix}}_{=\boldsymbol{H}_p}\boldsymbol{\xi}, \tag{25}$$

and have obtained the Jacobian $\boldsymbol{H}_p$ relating the position measured by the locator to the Lie algebra $\mathfrak{se}(3)$.

2) Range factor: With the result from (25), we only need to differentiate each term of (4) w.r.t $\boldsymbol{p}^n_{rb}$ about $\boldsymbol{\xi}=\boldsymbol{0}$ in order to obtain the desired Jacobians. The range measurement Jacobian is thus found as

$$\begin{aligned}
\boldsymbol{H}_\rho &= \frac{\partial h_\rho}{\partial \boldsymbol{\xi}^\wedge}\Big|_{\boldsymbol{\xi}=\boldsymbol{0}} = \frac{\partial h_\rho}{\partial \boldsymbol{p}^n_{rb}}\Big|_{\boldsymbol{\xi}=\boldsymbol{0}}\frac{\partial \boldsymbol{p}^n_{rb}}{\partial \boldsymbol{\xi}^\wedge}\\
&= \frac{1}{\|\hat{\boldsymbol{p}}^n_{rb}\|_2}(\hat{\boldsymbol{p}}^n_{rb})^\top\boldsymbol{H}_p \triangleq \boldsymbol{H}_c\boldsymbol{H}_p.
\end{aligned} \tag{26}$$

3) Azimuth factor: The term corresponding to the azimuth angle in (4) contains an arctangent, so in order to determine the Jacobian, we define a variable substitution $x(\boldsymbol{p}^n_{rb})$ and compute

$$\boldsymbol{H}_\Psi = \frac{\partial h_\Psi}{\partial \boldsymbol{p}^n_{rb}} = \frac{\partial h_\Psi}{\partial x}\frac{\partial x}{\partial \boldsymbol{p}^n_{rb}}\Big|_{\boldsymbol{\xi}=\boldsymbol{0}}\boldsymbol{H}_p. \tag{27}$$

The measured position can be written on the form $\boldsymbol{p}^n_{rb} = [p_x\ p_y\ p_z]^\top \triangleq \boldsymbol{p}$ such that $h_\Psi(\boldsymbol{p}) = \arctan(p_y/p_x)$. By defining $x \triangleq p_y/p_x$, such that $h_\Psi(x) = \arctan(x)$, we can write $\boldsymbol{H}_\Psi$ as

$$\boldsymbol{H}_\Psi = \frac{\partial h_\Psi}{\partial x}\frac{\partial x}{\partial \boldsymbol{p}}\Big|_{\boldsymbol{\xi}=\boldsymbol{0}}\boldsymbol{H}_p, \tag{28}$$

where

$$\frac{\partial h_\Psi(x)}{\partial x} = \frac{1}{1+x^2} = \frac{p_x^2}{p_x^2+p_y^2}, \tag{29}$$

is obtained directly from the definition of the arctangent and

$$\frac{\partial x}{\partial \boldsymbol{p}} = \begin{bmatrix}-\frac{p_y}{p_x^2} & \frac{1}{p_x} & 0\end{bmatrix}. \tag{30}$$

With this, we obtain the azimuth measurement Jacobian

$$\begin{aligned}
\boldsymbol{H}_\Psi &= \frac{p_x^2}{p_x^2+p_y^2}\begin{bmatrix}\frac{p_y}{p_x^2} & \frac{1}{p_x} & 0\end{bmatrix}\Big|_{\boldsymbol{\xi}=\boldsymbol{0}}\boldsymbol{H}_p\\
&= \frac{1}{\hat{p}_x^2+\hat{p}_y^2}\begin{bmatrix}-\hat{p}_y & \hat{p}_x & 0\end{bmatrix}\boldsymbol{H}_p \triangleq \boldsymbol{H}_c\boldsymbol{H}_p.
\end{aligned} \tag{31}$$

4) Elevation factor: $\boldsymbol{H}_\alpha$ is obtained by following the same method as for the azimuth factor with the only difference being the choice of x, which here will be given by the elevation term of (4)

$$x \triangleq \frac{-p_z}{\sqrt{p_x^2+p_y^2}}, \tag{32}$$

such that

$$\frac{\partial h_\alpha}{\partial x} = \frac{p_x^2+p_y^2}{p_x^2+p_y^2+p_z^2} = \frac{\|\bar{\boldsymbol{p}}\|_2^2}{\|\boldsymbol{p}\|_2^2}, \tag{33}$$

after some manipulations, and

$$\frac{\partial x}{\partial \boldsymbol{p}} = \begin{bmatrix} \frac{p_x p_z}{\|\bar{\boldsymbol{p}}\|_2^3} & \frac{p_y p_z}{\|\bar{\boldsymbol{p}}\|_2^3} & -\frac{1}{\|\bar{\boldsymbol{p}}\|_2} \end{bmatrix}, \tag{34}$$

where we have defined $\bar{\boldsymbol{p}} \in \mathbb{R}^2$ as the horizontal component of $\boldsymbol{p}$. With this, we obtain the elevation measurement Jacobian

$$\begin{aligned} \boldsymbol{H}_\alpha &= \frac{\|\bar{\boldsymbol{p}}\|_2^2}{\|\boldsymbol{p}\|_2^2} \begin{bmatrix} \frac{p_x p_z}{\|\bar{\boldsymbol{p}}\|_2^3} & \frac{p_y p_z}{\|\bar{\boldsymbol{p}}\|_2^3} & -\frac{1}{\|\bar{\boldsymbol{p}}\|_2} \end{bmatrix} \Big|_{\boldsymbol{\xi}=\boldsymbol{0}} \boldsymbol{H}_p \\ &= \frac{1}{\|\hat{\boldsymbol{p}}\|_2^2} \begin{bmatrix} \frac{p_x p_z}{\bar{\rho}} & \frac{p_y p_z}{\bar{\rho}} & -\bar{\rho} \end{bmatrix} \boldsymbol{H}_p \triangleq \boldsymbol{H}_c \boldsymbol{H}_p, \end{aligned} \tag{35}$$

where $\bar{\rho} \triangleq \sqrt{\hat{p}_x^2 + \hat{p}_y^2}$.

Appendix II
Error-state Kalman Filter

The baseline used for comparison estimator performance is a standard ESKF with error-state

$$\delta \boldsymbol{x} \triangleq [\delta \boldsymbol{p} \ \delta \boldsymbol{v} \ \delta \boldsymbol{\theta} \ \delta \boldsymbol{b}_{\text{acc}} \ \delta \boldsymbol{b}_{\text{gyro}}]^\top \in \mathbb{R}^{15} \tag{36}$$

with linearised kinematics obtained from [18]

$$\delta \dot{\boldsymbol{x}} = \boldsymbol{F}(\boldsymbol{x}) \delta \boldsymbol{x} + \boldsymbol{G}(\boldsymbol{x}) \boldsymbol{w} \tag{37}$$

where $\boldsymbol{F}$ and $\boldsymbol{G}$ are functions of the nominal state $\boldsymbol{x}$ and debiased IMU measurements. Assuming zero-order hold, the discrete-time transition matrix $\boldsymbol{F}_d$ and process noise covariance matrix $\boldsymbol{\mathcal{Q}}_d$ can then be obtained using Van Loan's formula [35]. The reader is referred to [21] for an overview of the ESKF algorithm, alternatively to the PDF on the ESKF in the GitHub repository accompanying this paper [17].

References

[1] P. D. Groves, *Principles of GNSS, inertial, and multisensor integrated navigation systems*, 2nd ed., ser. GNSS technology and application series. Boston: Artech House, 2013.

[2] A. Pinker and C. Smith, "Vulnerability of the GPS Signal to Jamming," *GPS Solutions*, vol. 3, no. 2, pp. 19–27, Oct. 1999.

[3] F. Kendoul and K. Nonami, "A visual navigation system for autonomous flight of micro air vehicles," in *2009 IEEE/RSJ Int. Conf. on Intelligent Robots and Systems*. St. Louis, MO, USA: IEEE, Oct. 2009, pp. 3888–3893.

[4] S. M. Albrektsen, A. Sagrov, and T. A. Johansen, "Navigation of UAV using phased array radio," in *2017 Workshop on Research, Education and Development of Unmanned Aerial Systems (RED-UAS)*. Linkoping: IEEE, Oct. 2017, pp. 138–143.

[5] S. M. Albrektsen, T. H. Bryne, and T. A. Johansen, "Robust and Secure UAV Navigation Using GNSS, Phased-Array Radio System and Inertial Sensor Fusion," in *2018 IEEE Conf. on Control Technology and Applications (CCTA)*, Aug. 2018, pp. 1338–1345.

[6] K. Gryte, T. H. Bryne, and T. A. Johansen, "Unmanned aircraft flight control aided by phased-array radio navigation," *J. Field Robotics*, vol. 38, pp. 532–551, 2021.

[7] ——, "Phased Array Radio Navigation: UAV Field Tests During GNSS Jamming," in *2024 Int. Conf. on Unmanned Aircraft Systems (ICUAS)*, Jun. 2024, pp. 586–593.

[8] M. Okuhara, T. H. Bryne, K. Gryte, and T. A. Johansen, "Elevation Angle Redundancy from Barometric Altitude in Multipath-affected Phased Array Radio Navigation of UAVs," in *2024 Int. Conf. on Unmanned Aircraft Systems (ICUAS)*. Chania - Crete, Greece: IEEE, Jun. 2024, pp. 1117–1124.

[9] M. L. Sollie, T. H. Bryne, K. Gryte, and T. A. Johansen, "Reducing Ground Reflection Multipath Errors for Bluetooth Angle-of-Arrival Estimation by Combining Independent Antenna Arrays," *IEEE Antennas and Wireless Propagation Letters*, vol. 22, no. 6, pp. 1391–1395, Jun. 2023.

[10] Direction Finding | Bluetooth® Technology Website. Accessed: 2024-05-09. [Online]. Available: https://www.bluetooth.com/learn-about-bluetooth/feature-enhancements/direction-finding/

[11] M. L. Sollie, K. Gryte, T. H. Bryne, and T. A. Johansen, "Outdoor Navigation Using Bluetooth Angle-of-Arrival Measurements," *IEEE Access*, vol. 10, pp. 88 012–88 033, 2022.

[12] S. M. Albrektsen, T. H. Bryne, and T. A. Johansen, "Phased array radio system aided inertial navigation for unmanned aerial vehicles," in *2018 IEEE Aerospace Conf.*, Mar. 2018, pp. 1–11.

[13] C. Forster, L. Carlone, F. Dellaert, and D. Scaramuzza, "On-Manifold Preintegration for Real-Time Visual–Inertial Odometry," *IEEE Transactions on Robotics*, vol. 33, no. 1, pp. 1–21, Feb. 2017.

[14] F. Dellaert and M. Kaess, "Factor Graphs for Robot Perception," *Foundations and Trends in Robotics*, vol. 6, no. 1-2, 2017.

[15] M. Brossard, A. Barrau, P. Chauchat, and S. Bonnabel, "Associating Uncertainty to Extended Poses for on Lie Group IMU Preintegration With Rotating Earth," *IEEE Transactions on Robotics*, vol. 38, no. 2, pp. 998–1015, Apr. 2022.

[16] A. Siemuri, E. Ahmadi, M. Elsanhoury, K. Selvan, P. Välisuo, H. Kuusniemi, and M. S. Elmusrati, "Optimal Robust Positioning Using Factor Graph," Sep. 2024, pp. 2684–2690.

[17] G. H. M. Sørensen and T. H. Bryne, "gsorensen/parnav_ins_sim." [Online]. Available: https://github.com/gsorensen/parnav_ins_sim

[18] J. Solà, "Quaternion kinematics for the error-state Kalman filter," Nov. 2017, arXiv:1711.02508 [cs].

[19] J. R. Carpenter and C. N. D'Souza, "Navigation Filter Best Practices," Apr. 2018, nTRS Author Affiliations: NASA Goddard Space Flight Center, NASA Johnson Space Center.

[20] K. Gryte, T. H. Bryne, S. M. Albrektsen, and T. A. Johansen, "Field Test Results of GNSS-denied Inertial Navigation aided by Phased-array Radio Systems for UAVs," in *2019 Int. Conf. on Unmanned Aircraft Systems (ICUAS)*. Atlanta, GA, USA: IEEE, Jun. 2019, pp. 1398–1406.

[21] M. Okuhara, T. H. Bryne, K. Gryte, and T. A. Johansen, "Phased Array Radio Navigation System on UAVs: In-Flight Calibration," *Journal of Intelligent & Robotic Systems*, vol. 109, no. 3, p. 51, Oct. 2023.

[22] J. Solà, J. Deray, and D. Atchuthan, "A micro Lie theory for state estimation in robotics," Dec. 2021, arXiv:1812.01537 [cs]. [Online]. Available: http://arxiv.org/abs/1812.01537

[23] T. D. Barfoot and P. T. Furgale, "Associating Uncertainty With Three-Dimensional Poses for Use in Estimation Problems," *IEEE Transactions on Robotics*, vol. 30, no. 3, pp. 679–693, Jun. 2014.

[24] M. Kaess, H. Johannsson, R. Roberts, V. Ila, J. Leonard, and F. Dellaert, "iSAM2: Incremental smoothing and mapping with fluid relinearization and incremental variable reordering," in *2011 IEEE Int. Conf. on Robotics and Automation*. Shanghai, China: IEEE, May 2011, pp. 3281–3288.

[25] T. Lupton and S. Sukkarieh, "Visual-Inertial-Aided Navigation for High-Dynamic Motion in Built Environments Without Initial Conditions," *IEEE Transactions on Robotics*, vol. 28, no. 1, pp. 61–76, Feb. 2012.

[26] C. Forster, L. Carlone, F. Dellaert, and D. Scaramuzza, "IMU Preintegration on Manifold for Efficient Visual-Inertial Maximum-a-Posteriori Estimation," in *Robotics: Science and Systems XI*. Robotics: Science and Systems Foundation, Jul. 2015.

[27] L. Carlone, Z. Kira, C. Beall, V. Indelman, and F. Dellaert, "Eliminating conditionally independent sets in factor graphs: A unifying perspective based on smart factors," in *2014 IEEE Int. Conf. on Robotics and Automation (ICRA)*, May 2014, pp. 4290–4297.

[28] F. Dellaert and GTSAM Contributors, "borglab/gtsam," May 2022. [Online]. Available: https://github.com/borglab/gtsam

[29] F. Gustafsson, *Statistical sensor fusion*, 3rd ed. Studentlitteratur, 2010.

[30] P. J. Huber, "Robust Estimation of a Location Parameter," *The Annals of Mathematical Statistics*, vol. 35, no. 1, pp. 73–101, Mar. 1964, publisher: Institute of Mathematical Statistics.

[31] K. Kafadar, "The Efficiency of the Biweight as a Robust Estimator of Location," *Journal of Research of the National Bureau of Standards*, vol. 88, no. 2, p. 105, Mar. 1983.

[32] Z. Zhang, "Parameter Estimation Techniques: A Tutorial with Application to Conic Fitting," *Image and Vision Computing*, vol. 15, no. 1, pp. 59–76, Jan. 1997.

[33] T. I. Fossen and T. Perez, "Marine Systems Simulator (MSS)," 2004, accessed: 2024-08-26. [Online]. Available: https://github.com/cybergalactic/MSS

[34] "Sensonor STIM300," accessed: 2024-05-22. [Online]. Available: https://safran-navigation-timing.com/product/stim300/

[35] C. Van Loan, "Computing integrals involving the matrix exponential," *IEEE Transactions on Automatic Control*, vol. 23, no. 3, pp. 395–404, Jun. 1978.